



Estimating the ELT's Differential Pistons with Deep Learning

Charleston Chauvet^{a, b}, Morgan Gray^a, Benoit Neichel^a, Maxime Dumont^{c, a, d},
Lisa Bardou^e, Jean-François Sauvage^{c, a}, and Olivier Beltramo-Martin^b

^aAix Marseille Université, CNRS, CNES, LAM, Marseille, France

^bSpaceAble, 75009 Paris, France

^cDOTA, ONERA, Université Paris Saclay, 91123 Palaiseau, France

^dINESCTEC, FEUP, Porto, Portugal

^eDepartment of Physics, Durham University, Durham, United Kingdom

ABSTRACT

High angular resolution requires large telescope apertures, which in turn often require segmented pupils. This is particularly true for large optical and infrared ground-based telescopes such as the Extremely Large Telescope (ELT). Due to its six large spiders and the segmented surface of its main mirror, the ELT's angular resolution is affected by the presence of pistons which cause phasing errors, thus the importance of measuring and correcting them. In addition to the pistons, the implementation of a fixed two-by-two Shack-Hartmann Wave Front Sensor (SHWFS), optical effects such as Turbulence Residuals (TR), Adaptive Optics RESiduals (AORES) and the main pupil's constant rotation also affect the ELT's Point Spread Function (PSF). Assuming in our study that each of the ELT's main pupil's six differential pistons follows a $[-\pi/2, \pi/2]$ uniform distribution (units in rad) and that the wavelength is set to $2.2 \mu\text{m}$, we show that convolutional Neural Networks (NN) offer a promising technique for accurately estimating each of the ELT's six differential pistons in the presence of TR. Indeed, each of the Root Mean Square Error (RMSE) values associated to these differential pistons are much lower than 0.1 rad, or equivalently about 35 nm, regardless of the pupil's rotation angle, except for configurations when a spider is close to a SHWFS axis by less than 3° of pupil rotation.

Keywords: Differential Pistons, Deep Learning, Point Spread Function, Extremely Large Telescope, Shack-Hartmann Wave Front Sensor, Turbulence Residuals, Adaptive Optics

1. INTRODUCTION

Ground-based astronomy is a scientific field where images with high angular resolution are essential for high-quality scientific return such as a greater advancement of astrophysical knowledge. The ELT is a large aperture telescope operated by the European Southern Observatory with a 39-meter main mirror composed of 798 segments.

Further author information:

E-mail: charleston.chauvet@lam.fr

Although a segmented pupil enables the telescope to offer a wider aperture, it also has a major drawback: each segment must be almost perfectly aligned with the others. More precisely, an alignment error of less than a fraction of the imaging wavelength is required for the large aperture to achieve full angular resolution.

For the ELT to achieve its theoretical angular resolution of 4 mas in the visible wavelength range, or equivalently 12 mas in the K-band, it must be equipped with powerful and cutting-edge Adaptive Optics (AO) systems capable of correcting wavefront aberrations up to a few tens of nm. Due to its six large spiders, each of 50 cm width, and the segmented surface of its main mirror, the ELT’s angular resolution is affected by the presence of pistons which cause phasing errors [7], hence the importance of measuring and correcting them. Since different pistons are applied on each of the pupil’s six petals, such phasing errors can be quantified as differences between two pistons that are applied on two adjacent petals. Therefore, measuring the phasing errors of the ELT’s pupil is equivalent to measuring these piston differences, also known as differential pistons. In addition to the pistons, the implementation of a two-by-two SHWFS, the main pupil’s permanent rotation, and optical effects such as TR and AORES also affect the ELT’s PSF.

The ELT’s differential pistons can potentially be estimated using a single focal plane image combined with well-known algorithms, such as asymmetric pupil phase diversity. However, these classical solutions are limited by mainly two phenomena. First, the AORES are slowly evolving and will not be averaged out enough in the image, challenging the phasing sensor to disentangle them from phasing speckles. Second, the ELT will also produce non-Kolmogorov phase residuals, also known as low wind effect, which are difficult to model and can be misinterpreted as phasing errors. Therefore, the core of this study is to explore non-linear methods to accurately estimate each of the ELT’s six differential pistons in the presence of a two-by-two SHWFS and optical effects regardless of the pupil’s rotation.

Deep Learning (DL) algorithms are well known and widely used to solve non-linear problems such as direct identification of image parameters and are therefore suitable for piston sensing [6, 2, 3]. In this work, we show that convolutional NN offer a promising technique for accurately estimating each of the ELT’s main pupil’s six differential pistons, given input PSF images affected by TR and the pupil’s constant rotation in the presence of a two-by-two SHWFS. Accurate estimation of the six differential pistons would then enable the reconstruction of the ELT’s PSF, which in turn would help to achieve the ELT’s expected theoretical angular resolution. A PSF image simulator with some routines inspired from the P3 library code [1] was designed to simulate a large amount of realistic PSF image samples, while the training, validation, and testing of the NN were carried out using the DEEPLOOP code [4].

First, we will review the instrumentation setup. Then, we will explain the optical effects that affect the ELT’s PSF, our methodology, and the DL framework we used to estimate the differential pistons. Finally, we will present and discuss the estimation results in the cases of PSF images without and with TR.

2. INSTRUMENTATION SETUP

2.1 Pupil, spiders, petals, segments, rotation

To support the ELT’s 39-meter main pupil, six spiders, each of 50 cm wide, have been installed. From the incoming wavefront’s perspective, these spiders divide the pupil’s surface area into six equally sized petals. Each petal contains 133 segments, adding up to a total of 798 segments for the entire pupil. In addition, the pupil’s permanent rotation is an important feature that sets the ELT apart from other large telescopes. The instrumentation setup and conventions we adopted in this work are presented in Fig. 1.

2.2 Full and differential pistons

The presence of large spiders and the segmentation of the ELT’s pupil imply the presence of pistons which degrade the angular resolution, hence the importance of measuring the phasing errors caused by these pistons. We first distinguish two concepts: full and differential pistons.

We define a full piston as the piston value applied on a single petal, while we define a differential piston as the difference between two piston values being applied on two adjacent petals. Since the ELT’s pupil experiences full pistons values that vary from one petal to another, the phasing errors can be defined as differences between two

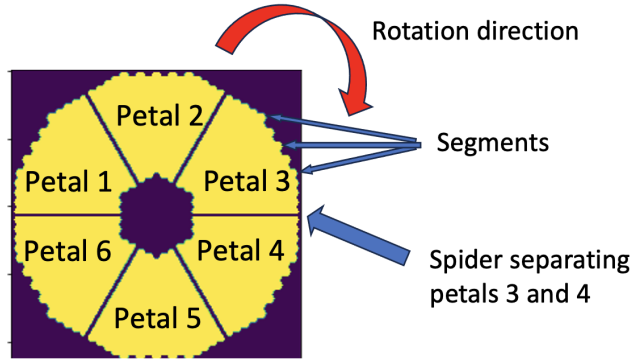


Figure 1. ELT's rotating and segmented main pupil with a surface area divided into six petals by six spiders.

piston values that are applied on two adjacent petals, that is a total of six differential pistons. The six full piston values are represented together by what we call a full phase map as shown in Fig. 2 a). The distinction between a full and a differential piston is illustrated in Fig. 2 b). For notation purposes, we define the convention that the differential piston between adjacent petals i and j , with $i < j$, is denoted by $p_j - p_i$.

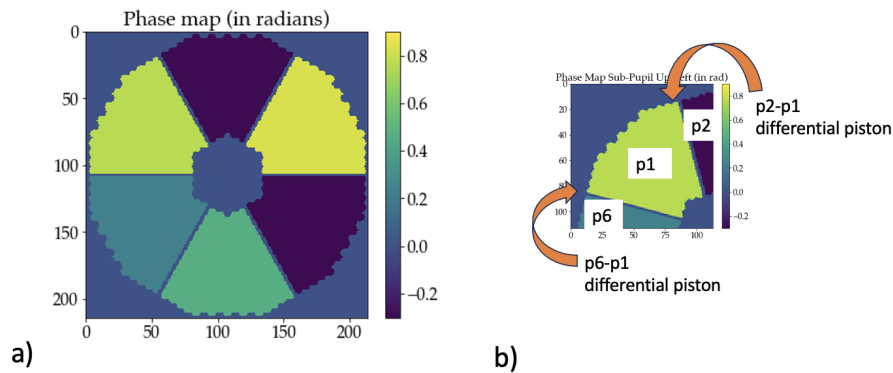


Figure 2. a) Full phase map sample (0° rotation) b) Full and differential pistons in the upper left part of the ELT's main pupil (15° rotation).

2.3 Instrumentation constraints

A two-by-two SHWFS was installed to correct the optical aberrations affecting the ELT's PSF. As illustrated in Fig. 3, such two-by-two SHWFS can be schematically represented as two perpendicular axes whose intersection point coincides with the main pupil's center and which divide the pupil's surface area into four equally sized ones. It is worth indicating that while the pupil constantly rotates, the SHWFS axes are fixed. Even though a two-by-two SHWFS is one of the most efficient wavefront sensors, it also has two major setbacks that are specific to our project and thus directly impacted our methodology: the permanent superposition of the two SHWFS axes with at least two petals and the periodic superposition of one SHWFS axis with two aligned spiders.

2.3.1 Superposition of the SHWFS axes with petals

The first constraint implied by the presence of a two-by-two SHWFS is that the two SHWFS axes will be superposed with four petals for most rotation angles. This configuration does not happen whenever one of the SHWFS axes is superposed with two aligned spiders, that is for every 30° rotation starting from the configuration shown in Fig. 3 a). In such cases, the second SHWFS axis will be superposed with two directly opposite petals. More details will follow in subsection 2.3.2. Fig. 3 b) shows a configuration where the two SHWFS axes are superposed with four petals. A direct consequence of such superposition configurations is that it becomes

impossible to derive a PSF image via Fourier optics from any phase map whose corresponding pupil surface area intersects with at least one SHWFS axis.

2.3.2 Superposition of one SHWFS axis with two spiders

The second constraint implied by the presence of a two-by-two SHWFS is that one SHWFS axis will be superposed with two aligned spiders for every 30° rotation starting from the configuration shown in Fig. 3 a). In such cases, it becomes impossible to estimate the two differential pistons that are located at the superposition of a SHWFS axis with two aligned spiders. This periodic feature implies two considerations. On the one hand, we know that it is technically impossible to estimate each of the six differential pistons for every rotation angle of the pupil. On the other hand, we can show that we can no longer afford to have complete PSF images that are derived via Fourier optics from a full phase map.

To explain the second part, let us consider, as an example, the configuration shown in Fig. 3 a). In such case, it is possible to estimate the p2-p1, p3-p2, p5-p4, and p6-p5 differential pistons as the corresponding spiders are not superposed with any SHWFS axis. On the contrary, the p6-p1 and p4-p3 ones cannot be estimated due to the superposition of the SHWFS's x-axis with the spider separating petals 6 and 1 and the one separating petals 4 and 3. If we were to consider the full phase map to derive the PSF, then we would have no information about the phasing error between the upper semi-pupil constituted by petals 1, 2 and 3, and the lower semi-pupil constituted by petals 4, 5 and 6. In other words, the big differential piston which consists in the p6-p1 and p4-p3 differential pistons aligned together cannot be estimated. Therefore, the p1, p2 and p3 full pistons are independent from the p4, p5 and p6 ones. Consequently, the six differential pistons cannot be simultaneously estimated from a single PSF image of the same size as for the pupil. Thus, estimating the differential pistons of the upper semi-pupil on the one hand and then estimating the ones of the lower semi-pupil on the other hand is required.

Finally, given the first constraint described in subsection 2.3.1 and that the fixed SHWFS axes divide the pupil surface area into four equally sized, independent, and four times smaller surface areas, we decided to work with the four sub-pupils that are delimited by the SHWFS axes. An illustration of these four sub-pupils can be further found in Fig. 6. We can only afford obtaining four smaller PSF images each derived from the corresponding sub-pupils, instead of one full PSF image derived from the full pupil.

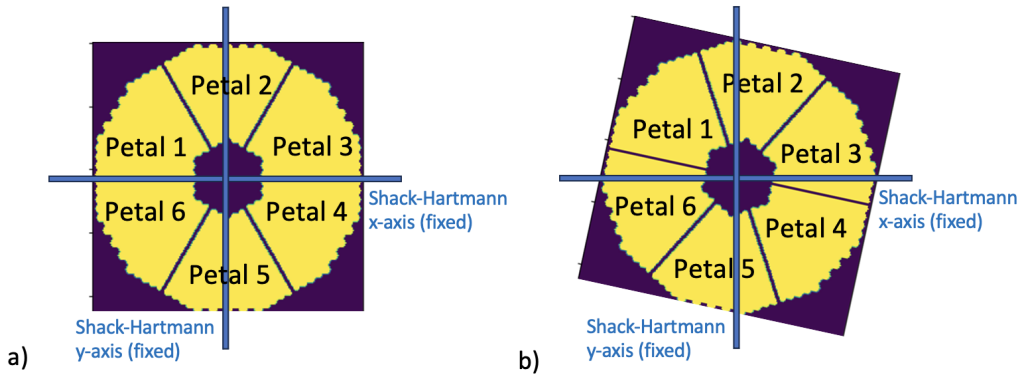


Figure 3. a) Configuration with the SHWFS x-axis superposed with two spiders and two petals (0° rotation), b) Configuration with the two SHWFS axes superposed with four petals (15° rotation).

3. METHODOLOGY

3.1 Optical effects

The ELT's PSF can be affected by optical effects, namely TR and AORES. TR, also known as pure fitting error, affect the PSF's high spatial frequencies while AORES affect the low spatial ones. As both TR and AORES can have different amplitudes, we define an optical effect configuration as a combination of two values: a certain TR amplitude and a certain AORES amplitude. Given the wide range of possible TR and AORES amplitudes,

the total number of possible optical effect configurations is very large. Fig. 4 shows full phase maps with three different optical effect configurations.

In the presence of TR, the morphology of the PSF will not be changed within the AO correction radius illustrated by the black circle which can be seen in the two upper images of Fig. 5 b), but the diffraction peak will be lower, that is the Strehl ratio is reduced.

However, in the presence of AORES, these residuals will introduce speckles within the correction radius and may affect the PSF’s morphology. The presence of AORES represents a more realistic case, with level of corrections like what we expect for instance for HARMONI [5], but at the same time constitutes a challenging case as the residual speckles appears in the same position on the PSF where the petaling signal is. This will then be the ultimate test of the robustness of the method and will be addressed in future work.

To have a better understanding of the potential of NN at estimating the ELT’s differential pistons, we will first conduct some tests with PSF images that are obtained in ideal conditions, that is with neither TR nor AORES. Once the first tests will be completed on a perfect diffraction limited case, the next step will be to introduce some TR post-AO correction. The estimation of the differential pistons in the presence of AORES is out of the current study’s scope.

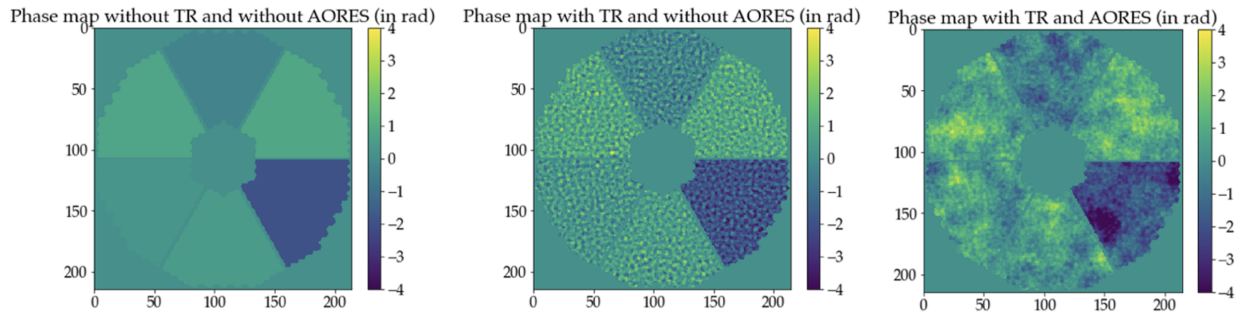


Figure 4. From left to right: ELT full phase map with neither TR nor AORES, with TR only, with both TR and AORES.

3.2 Sub-PSF properties

In this subsection, we describe the two main sub-PSF image properties that will enable us to simplify our methodology, that is the central crop size of the sub-PSF images and the symmetry between non-adjacent sub-pupils.

3.2.1 Sub-PSF image central crop size

It is well understood that most of the determining optical information and energy characterizing a full PSF image is generally contained within its center. This is also true for sub-PSF images. Therefore, directly feeding sub-PSF images as inputs to the NN is not essential and would otherwise require considerably long training times that steeply increase with the sub-PSF images’ size. Given that our study is conducted exclusively with sub-PSF images of 214 by 214 pixels, we first decided to only keep the center of each of these sub-PSF images to get smaller sub-PSF images of size 33 by 33 pixels and to conduct tests only using this image size. For more clarity, we will from now on denote any sub-PSF image that has not been yet centrally cropped as a full sub-PSF image.

However, it is also known from a DL perspective that feeding NN with larger amounts of information such as bigger-sized cropped sub-PSF images is generally more beneficial. Indeed, we want to let the NN identify on their own features in larger centrally cropped sub-PSF images that are potentially relevant for better estimating the differential pistons and which are not captured by smaller centrally cropped sub-PSF images. Fig. 5 shows full sub-PSF image samples with their respective centrally cropped sub-PSF images of 97 by 97 pixels and of 33 by 33 pixels, and subjected to different three different optical effect configurations. For simplicity, we only show sub-PSF images that are derived from the Up-Right sub-pupil as we observe the same properties for the Up-Left one.

Furthermore, although out of this study’s scope, it is worth noticing that, since our ultimate goal is to develop a framework able to estimate the differential pistons regardless of the TR and AORES amplitudes, a 97 by 97 pixels centrally cropped sub-PSF image for example is much more appropriate compared to a 33 by 33 pixels one as we can see, from Fig. 5, that it is much easier to distinguish the different optical effect configurations for larger centrally cropped images compared to smaller ones. One of our ultimate objectives would be to develop NN such that they can estimate each of the differential pistons in the Up-Right and Up-Left cases regardless of the pupil’s rotation angle and the TR and AO residual amplitudes. Therefore, after generating and conducting tests on centrally cropped sub-PSF images of size 33 by 33 pixels exclusively, we finally decided to generate and conduct tests on centrally cropped sub-PSF images of size 97 by 97 pixels.

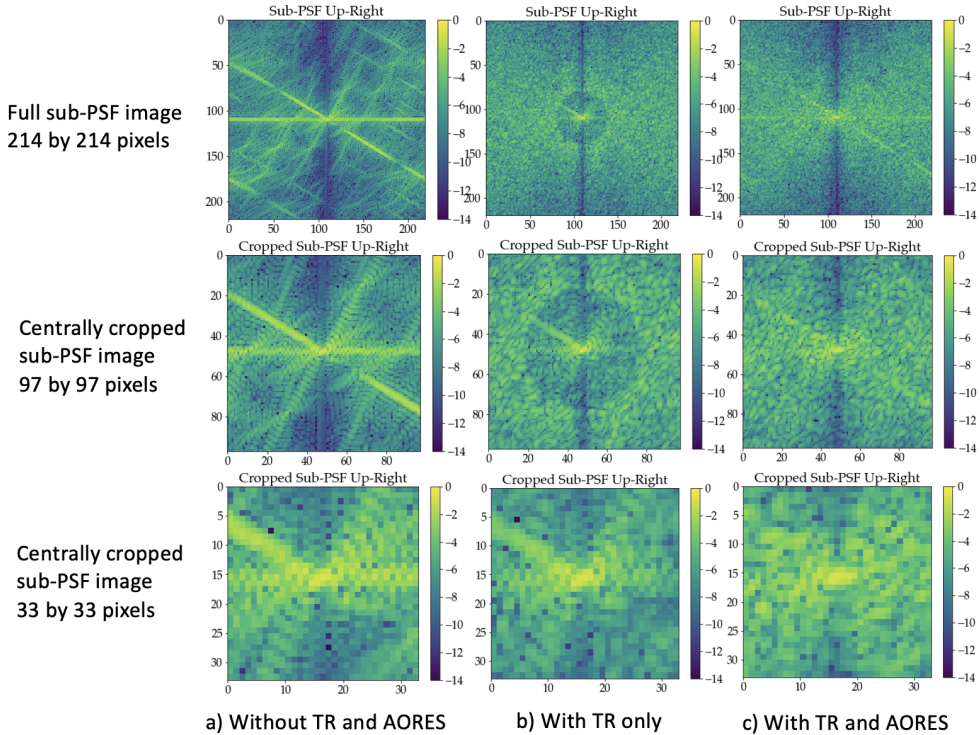


Figure 5. a) Up-Right full sub-PSF 214 by 214 pixels image sample and the corresponding 97 by 97 pixels and 33 by 33 pixels centrally cropped sub-PSF images with neither TR nor AORES, b) With TR only, c) With both TR and AORES (images in logarithmic scale).

3.2.2 Non-adjacent sub-pupil symmetry

As mentioned in subsection 2.3.2, we cannot afford obtaining full PSF images that are derived using Fourier optics from the full phase map. Instead, we need to consider four sub-pupils one by one, which are illustrated in Fig. 6.

Interestingly, we observe that non-adjacent sub-pupils are symmetrical, regardless of the pupil’s rotation angle. In other words, let us take the example of the Up-Right sub-pupil. If we can design a NN that estimates the p3-p2 differential piston given a sub-PSF image obtained from the phase map associated with the Up-Right sub-pupil, then we do not need to train another NN that estimates the p6-p5 differential piston in the Down-Left sub-pupil as we can use the previous one already trained for the Up-Right sub-pupil to estimate it. The same principle applies for the Up-Left and Down-Right sub-pupils. In that case, being able to accurately estimate the p6-p1 and p2-p1 differential pistons means that we can also estimate the p4-p3 and p5-p4 ones respectively. Therefore, in our methodology, we will only focus on the Up-Left and Up-Right sub-pupils.

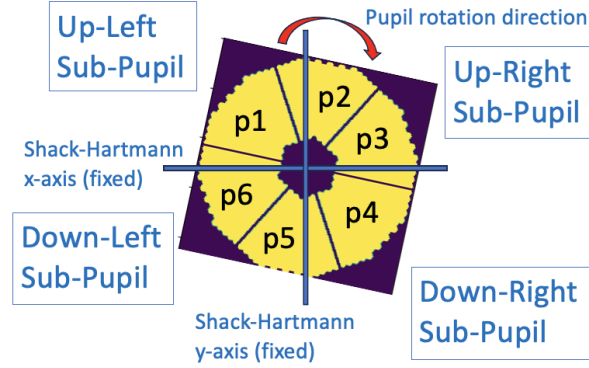


Figure 6. ELT's four sub-pupils delimited by the two-by-two SHWFS.

3.3 Steps

As explained in subsection 2.3, the installation of a two-by-two SHWFS completely modifies the initial instrumentation setup. It becomes impossible to generate complete PSF images from the full pupil, and each independent sub-pupil generates its corresponding sub-PSF images that are four times smaller compared to the complete PSF image that would have been obtained in the absence of the SHWFS. Furthermore, the symmetry between opposite sub-pupils implies that we only need to estimate the differential pistons present in the Up-Right and Up-Left sub-pupils.

We first decided to train one NN for each sub-pupil, that is one to estimate the Up-Right sub-pupil's p3-p2 differential piston and another one to estimate both the p6-p1 and p2-p1 differential pistons in the Up-Left sub-pupil simultaneously. Our tests concluded that estimating each differential piston in the UL-Left sub-pupil separately yields more accurate estimations. Consequently, we decided to train a first NN for the p3-p2 differential piston, a second one for p6-p1, and a third one for p2-p1, summing up to a total of three NN in our study.

Given the above constraints and properties, the steps we followed as part of our methodology are described as follows:

- 1) We train a NN that takes, as input, any sub-PSF image obtained from the Up-Right sub-pupil, and estimates, as output, the p3-p2 differential piston.
- 2) We train a NN that takes, as input, any sub-PSF image obtained from the Up-Left sub-pupil, and estimates, as output, the p6-p1 differential piston.
- 3) We train a NN that takes, as input, any sub-PSF image obtained from the Up-Left sub-pupil, and estimates, as output, the p2-p1 differential piston.
- 4) Due to the symmetry of non-adjacent sub-pupils, the three differential pistons left can be estimated using the three NN developed in steps 1), 2) and 3).
- 5) Due to the rotation of the pupil and its 30° periodicity implied by the presence of six spiders and two SHWFS axes, it is sufficient to train the NN on sub-PSF images with rotation angles ranging from 0° to 30° .
- 6) Due to the impossibility of estimating differential pistons when one SHWFS axis is superposed with two aligned spiders, some differential pistons cannot be estimated when the pupil rotation angle is a multiple of 30° starting from the configuration shown, for example, in Fig. 3 a). Consequently, we can only train NN with sub-PSF images that have rotation angles between 1° and 29° . Furthermore, due to the large number of rotation angles in this range and since our problem is a regression task, we will only train NN in the $[1^\circ, 29^\circ]$ range with an increment of 1° .

Fig. 7 shows a summary of our approach.

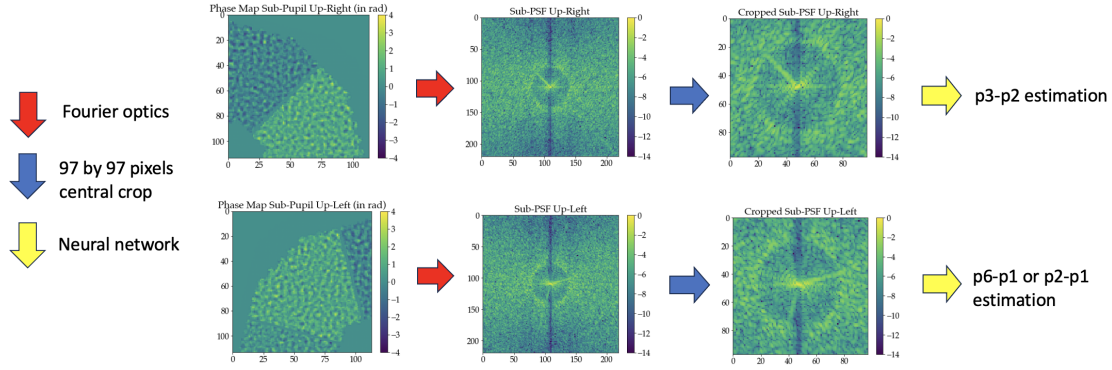


Figure 7. From the sub-pupil phase maps (inputs) to the estimation of the differential pistons (outputs) (sub-PSF images in logarithmic scale).

3.4 Deep Learning

In this subsection, we will describe the data and the NN architectures used in our study.

3.4.1 Data

Before training our NN to estimate the ELT's six differential pistons, we have designed a PSF image generator that can simulate realistic sub-PSF images of the ELT regardless of TR and AORES as the pupil's rotation angle. In particular:

- The six full piston values of the ELT's full pupil are generated from a $[-\pi/2, \pi/2]$ uniform distribution.
- The sub-PSF images are Nyquist-sampled.
- The datasets contain sub-PSF image samples with rotation angles ranging from 1° to 29° with 1° increments.
- The validation set contains a total number of sub-PSF image samples equal to 20% of the total number in the training set.
- Regardless of the differential piston to estimate as well as the optical effect configuration, we created 29 datasets such that each of them contains a total of 3000 test sub-PSF image samples that are all obtained from a single rotation angle within the $[1^\circ, 29^\circ]$ range, adding up to a total of 87 000 test samples. As such, each trained NN in our study is evaluated on a total of 3000 unseen sub-PSF image samples for each rotation angle in the $[1^\circ, 29^\circ]$ range with 1° increments. The test set performances will be presented in subsection 4.2 and subsection 4.3.

The numbers of training sub-PSF image samples for each optical effect configuration and differential piston are given in Tab. 1.

Table 1. Quantities of training sub-PSF image samples depending on the differential piston and the presence of TR.

Presence of TR	Differential Piston	Number of training samples
False	p3-p2	200 000
False	p6-p1	200 000
False	p2-p1	400 000
True	p3-p2	400 000
True	p6-p1	400 000
True	p2-p1	400 000

3.4.2 Neural Networks

Since the data to be fed as input to our NN are images, a convolutional NN is best suited to our applications compared to, for example, simple dense layers that are computationally too expensive due to the large number of neuron connections. We tested state-of-the-art architectures that work well for other types of computer vision applications. Among them, Visual Geometry Group NN (VGGNets) are very well-known model architectures. Since each optical effect configuration and each sub-pupil represents a completely new case, we need to train a NN for each differential piston (p3-p2, p6-p1, p2-p1) and each individual optical effect configuration (without TR and with TR), summing up to a total of six NN.

After conducting tests exclusively with VGGNets, we finally decided to use other types of architectures such as Residual NN (ResNets) as they are also appropriate for our current application, with the specificity that they allow, through their cut layers and identity connections, to train much deeper NN architectures, which are essential for trying to estimate harder cases such as in the context of PSF images that are not only affected by TR but also by AORES in a future work.

Furthermore, since we know by how much degrees the main pupil rotates at any given time, one of the ways to make the NN more robust is to use that piece of information efficiently by incorporating it into our model architectures. Although a series of data reduction operations in the convolutional layers of our NN is performed to further reduce the input sub-PSF image size, flattening the image yields many neurons that all contain crucial information. Determining where the rotation angle information should be concatenated in the NN architecture is thus crucial. Indeed, if such a rotation angle is concatenated with the output of the flatten layer, then the weight of the rotation angle value will be negligible compared to the huge number of neurons obtained through the flatten layer. On the contrary, if such rotation angle information is concatenated with the output of, for example, the first dense layer, then the weight of the rotation angle will be much more important and thus contribute more to the robustness of the differential piston estimations.

Our tests have been conducted using two different ResNet architectures which we denote by ResNet1 and ResNet2 hereafter. The architecture of ResNet1 is shown in Fig. 8 and only features Rectified Linear Unit (ReLU) activation functions that are omitted in the figure for simplicity. Given a centrally cropped sub-PSF image of size 97 by 97 pixels as input, ResNet1 consists in two convolutional layers of shape (97, 97, 32). The output is fed as input not only to a first block of two convolutional layers of shape (49, 49, 64) but also to a cut layer of shape (49, 49, 64) whose output is added to the input of the second convolutional layer's activation function within that first block. That first block's output is then not only fed as input to a second block of two other convolutional layers of shape (49, 49, 64) but also added to the output of the second convolutional layer's activation function within that second block. The architecture continues with two blocks of the same pattern followed by a max pooling layer. Once the image gets a (7, 7, 128) shape, a flatten layer is used, followed by two dense layers of 16 neurons each and a final dense layer which outputs a single differential piston value. For the rotation angle value to be considered, that information is concatenated with the 16 neurons of the first dense layer. ResNet2 is similar to ResNet1 except that we add two extra blocks of two convolutional layers of shape (13, 13, 256) with the associated cut layer and identity connections following the same pattern as in the blocks within ResNet1. The NN hyperparameter values vary depending on the differential piston to estimate and the optical effect configuration.

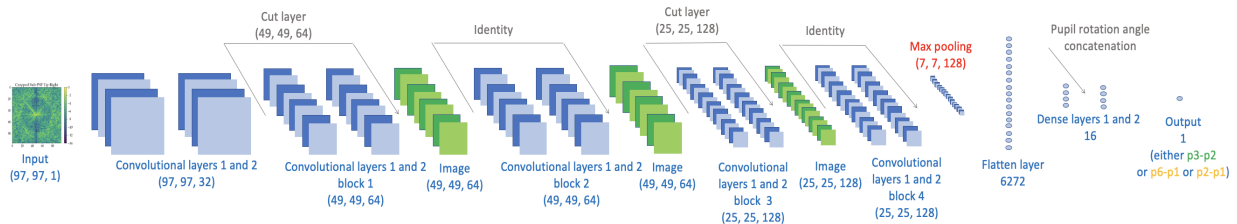


Figure 8. ResNet1 architecture used to estimate a single differential piston from centrally cropped sub-PSF images of 97 by 97 pixels.

4. RESULTS

4.1 Performance analysis

To evaluate the performance of our differential piston estimations, we need both quantitative and qualitative performance criteria to measure how close the estimated differential piston values are from the ground-truth ones. Due to our DL-focused method, the RMSE is a widely used metric. We will also reconstruct the estimated sub-PSF images from the estimated differential pistons, and then compare how close the ground-truth and estimated sub-PSF images are. As mentioned in subsection 3.1, we will consider two optical effect configurations: first without TR for both the Up-Right and Up-Left sub-pupils to evaluate the relevance of NN for estimating the ELT's differential pistons, and then with TR for both the Up-Right and Up-Left sub-pupils. For each considered case, we will provide both the differential piston RMSE as a function of the main pupil's rotation angle, as well as reconstructed sub-PSF images.

4.1.1 Root Mean Square Error

Although we do not have a clear threshold value above which the RMSE is considered too high, we set a representative threshold to be equal to 0.1 rad given that the six full piston values of the ELT's full pupil are generated from a $[-\pi/2, \pi/2]$ uniform distribution. As the wavelength is set to $2.2 \mu\text{m}$, this threshold is equivalent to around 35 nm. The goal is to obtain RMSE values that are systematically below 35 nm for each rotation angle value in the $[1^\circ, 29^\circ]$ range with a 1° increment.

4.1.2 Sub-PSF image reconstruction

Since sub-PSF images are obtained through Fourier optics from the corresponding sub-pupil phase maps, one way to check the performance of our NN in estimating the differential pistons is to reconstruct the sub-PSF images based on the estimated differential piston values, and then compare these estimated images with the real ones which are derived from the ground-truth differential piston values. The image differences between the estimated and ground-truth sub-PSF images are called the sub-PSF image residuals, and thus we want these residuals to be as small as possible. All the sub-PSF image reconstructions will be displayed in logarithmic scale.

4.2 Results on sub-PSF images without Turbulence Residual

Fig. 9 shows the differential piston RMSE values for both the Up-Right and Up-Left sub-pupils in the absence of TR. As described in 4.1.1, the values are given in nm for each rotation angle within the $[1^\circ, 29^\circ]$ range with a 1° increment. The red dotted line corresponds to the 0.1 rad threshold described earlier.

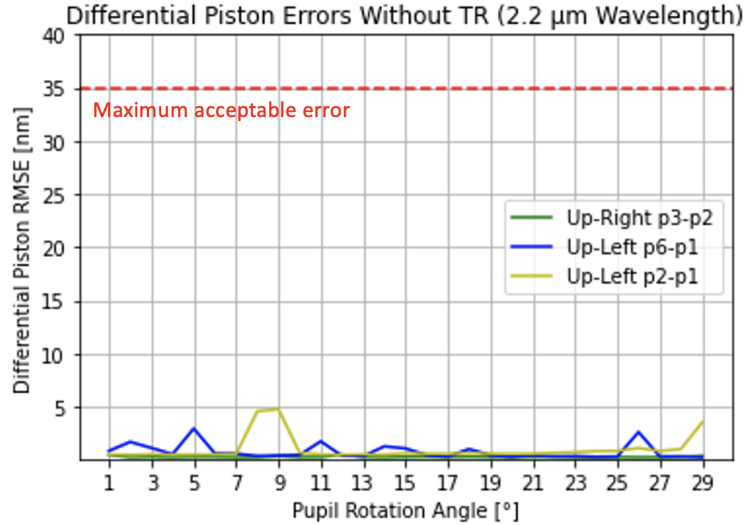


Figure 9. Differential piston estimation errors as a function of the pupil's rotation angle without TR.

In the absence of TR, we observe an overall RMSE value of 0.3 nm regardless of the pupil’s rotation angle for the p3-p2 differential piston present in the Up-Right sub-pupil.

Regarding the Up-Left sub-pupil, the RMSE values of both the p6-p1 and p2-p1 are also very low. Although not yet deeply analyzed, the fluctuations of both the p6-p1 and p2-p1 RMSE values are thought to be statistical artefacts as we fed our NN with a limited amount of sub-PSF image samples for each of the 29 rotation angles within the $[1^\circ, 29^\circ]$ range. Indeed, if we consider the p6-p1 differential piston as an example, we have a training set of 200 000 Up-Left sub-PSF image samples containing an equal number of samples for each rotation angle in the $[1^\circ, 29^\circ]$ range, as indicated in Tab. 1. Therefore, for each rotation angle, the total number of samples is roughly equal to 6900 which is generally not huge for computer vision tasks. Similarly, although we fed a NN with 400 000 training images to estimate the p2-p1 differential piston as also indicated in Tab. 1, a number of 13 800 samples is still not huge enough to achieve equally good performances for each rotation angle in the $[1^\circ, 29^\circ]$ range. Future work will aim at addressing these fluctuations. However, it is worth noting that the highest RMSE fluctuation reaches no more than 5 nm, which shows that the differential piston estimations for both the p6-p1 and p2-p1 differential pistons are very accurate. Furthermore, although not yet deeply analyzed, trying to achieve equally good performances for each rotation angle may be very difficult in such regime, especially without a huge amount of sub-PSF image samples for each rotation angle.

In both Up-Right and Up-Left cases in the absence of TR, we observe that it is possible to estimate each of the differential pistons accurately regardless of the main pupil’s rotation angle.

Fig. 10 and Fig. 11 show samples of sub-PSF images that have been reconstructed based on the estimated differential piston values and the ground-truth ones, as well as their residuals, for the Up-Right and Up-Left sub-pupils respectively in the absence of TR. We observe that in both cases, the true and estimated reconstructed sub-PSF images are very close to each other. This is expected as the estimated differential piston’s RMSE values for both the Up-Right and Up-Left sub-pupils are very low.

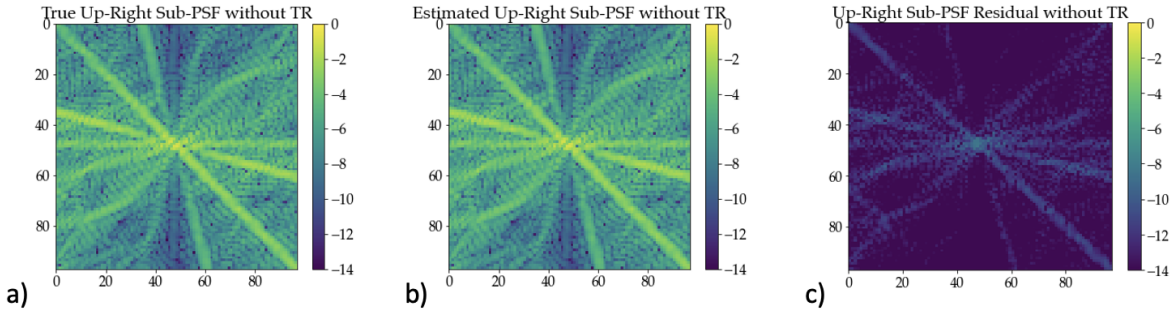


Figure 10. a) Ground-truth, b) Estimated, c) Residual of a sub-PSF image sample derived from the Up-Right sub-pupil with a 15° rotation in the absence of TR (logarithmic scale).

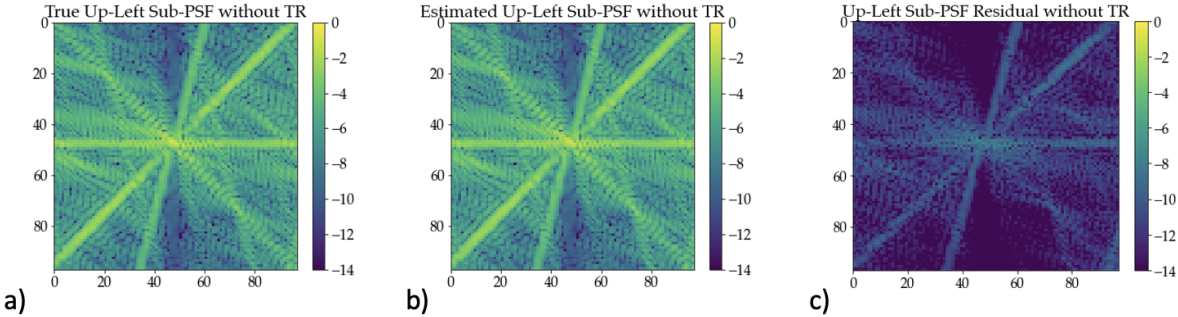


Figure 11. a) Ground-truth, b) Estimated, c) Residual of a sub-PSF image sample derived from the Up-Left sub-pupil with a 15° rotation in the absence of TR (logarithmic scale).

4.3 Results on sub-PSF images affected by Turbulence Residuals

Similarly to subsection 4.2, Fig. 12 shows the differential piston RMSE values for both the Up-Right and Up-Left sub-pupils but this time in the presence of TR. Although we observe, for the Up-Right sub-pupil, a RMSE gap of a factor of 10 compared to the previous Up-Right case without TR, the p3-p2 differential piston RMSE values are still very low as they are globally around 2.5 nm regardless of the pupil’s rotation angle.

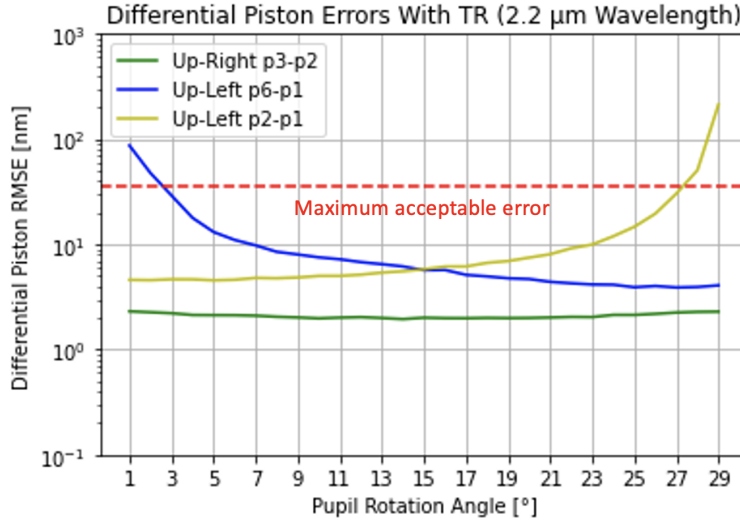


Figure 12. Differential piston estimation errors as a function of the pupil’s rotation angle with TR (logarithmic scale).

Regarding the Up-left sub-pupil case, we observe that, despite the RMSE gap compared to the previous Up-Left case without TR, the RMSE values in the [3°, 27°] range for both the p2-p1 and p6-p1 differential pistons are below the threshold we have set. Such a gap is expected as it is now much more difficult to estimate these two differential pistons as some TR affect the sub-PSF images.

However, we observe that the p6-p1 differential piston is poorly estimated when the rotation angle approaches 1° while the p2-p1 one experiences the same as the rotation angle gets close to 29°. More precisely, the p2-p1 RMSE steeply increases as the rotation angle approaches 29° while the p6-p1 RMSE steeply decreases as the rotation angle gets further away from 1°. These poor performances at extreme rotation angle values are thought to originate from the impossibility to determine both the p6-p1 and p2-p1 differential pistons when the rotation angle is equal to 0° and 30° respectively starting from the configuration shown, for example, in Fig. 3 a). Following that same configuration, since the instrumentation setups formed by the pupil, its spiders and the SHWFS at a pupil’s rotation angle of 1° and 2° quite resemble to the configuration with a pupil’s rotation angle of 0°, the pupil’s surface area between the SHWFS’s x-axis and the spider separating petals 1 and 6, which is a small part of petal 6, is very small. Consequently, the p6 piston value that is applied on that very small petal area has a very poor determining contribution for our NN to accurately estimate the p6-p1 differential piston in the [1°, 2°] range, which makes the estimation much harder compared to angles in the [3°, 29°] range. A similar reasoning applies for the p2-p1 differential piston. Future work will aim at addressing these poor estimations for extreme rotation angles.

Similarly to subsection 4.2, Fig. 13 and Fig. 14 show that the estimated reconstructed sub-PSF images for the Up-Right and Up-Left sub-pupils respectively are close to the ground-truth ones within the center, despite of more significant residuals and differential pistons estimations which are less accurate compared to the case without TR for both the Up-Right and Up-Left sub-pupils.

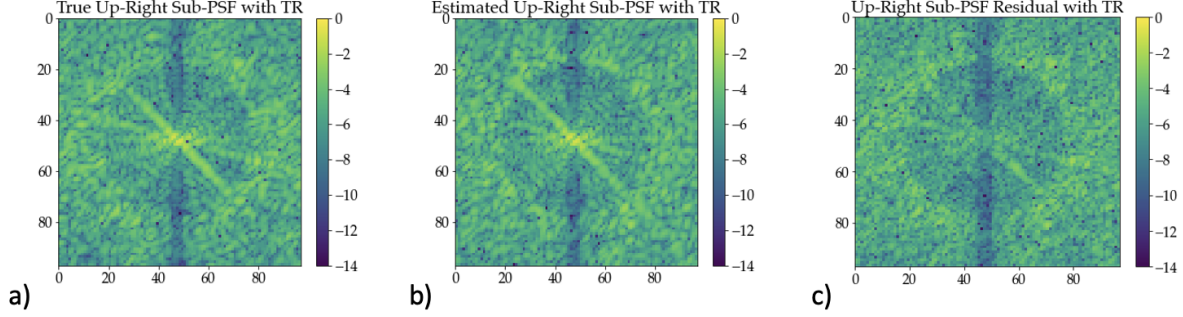


Figure 13. a) Ground-truth, b) Estimated, c) Residual of a sub-PSF image sample derived from the Up-Right sub-pupil with a 15° rotation in the presence of TR (logarithmic scale).

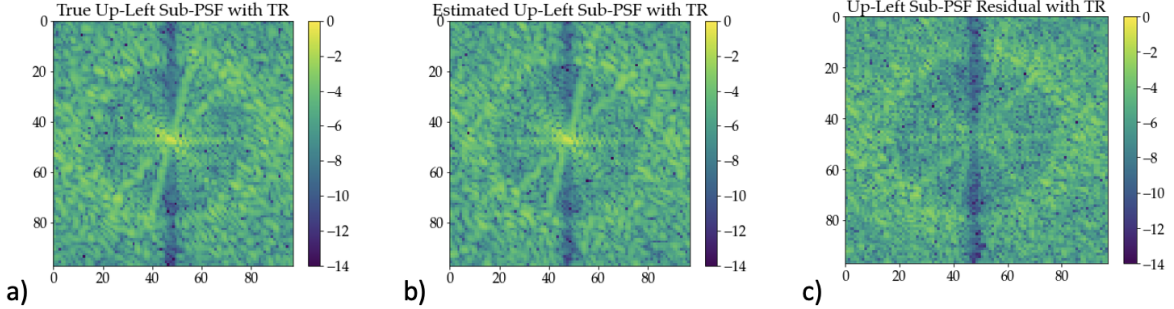


Figure 14. a) Ground-truth, b) Estimated, c) Residual of a sub-PSF image sample derived from the Up-Left sub-pupil with a 15° rotation in the presence of TR (logarithmic scale).

5. CONCLUSIONS

Despite instrumentation constraints caused by the installation of a two-by-two SHWFS on the ELT, we have shown that convolutional NN can be used for accurately estimating each of the ELT’s main pupil’s six differential pistons in the presence of TR and regardless of the pupil’s rotation angle. The task of estimating a specific differential piston is however made impossible whenever a SHWFS axis and the spider associated to that differential piston are superposed. In terms of performance, assuming in our study that each of the six differential pistons follows a $[-\pi/2, \pi/2]$ uniform distribution and that the wavelength is set to $2.2 \mu\text{m}$, the differential piston errors are always less than 0.1 rad, or equivalently about 35 nm, except for cases when a SHWFS axis is nearly superposed with a spider. We aim at addressing this last issue by training more complex NN model architectures such as Inception Networks to try decreasing estimation errors for extreme rotation angles of the pupil. We also aim at enhancing model robustness by training several NN for a single differential piston so that each of them estimates it for a smaller range of rotation angles. Finally, future work will mainly consist in the generalisation of this current study by testing the feasibility of estimating differential pistons in the presence of both TR and AORES regardless of their amplitudes.

References

- [1] O. Beltramo-Martin. *P3*. <https://github.com/astro-tiptop/P3>.
- [2] M. Dumont et al. *Deep learning for adaptive optics psf prediction*. 2021 <https://ao4astro2.sciencesconf.org/resource/page/id/5>.
- [3] M. Dumont et al. “Deep learning for space-borne focal-plane wavefront sensing”. In: *Space Telescopes and Instrumentation 2022: Optical, Infrared, and Millimeter Wave*. Ed. by L.E. Coyle, S. Matsuura, and M.D. Perrin. Vol. 12180. Proc. SPIE. 2022.

- [4] M. Gray et al. “DEEPLoop: DEEP Learning for an Optimized adaptive Optics Psf estimation”. In: *Adaptive Optics Systems VIII*. Ed. by L. Schreiber, D. Schmidt, and E. Vernet. Vol. 12185. Proc. SPIE. 2022.
- [5] B. Neichel et al. “The adaptive optics modes for HARMONI: from Classical to Laser Assisted Tomographic AO”. In: *Adaptive Optics Systems V*. Ed. by E. Marchetti, L.M. Close, and J.-P. Véran. Vol. 9909. Proc. SPIE. 2016.
- [6] F. Rossi et al. “Machine learning techniques for piston sensing”. In: *Adaptive Optics Systems VIII*. Ed. by L. Schreiber, D. Schmidt, and E. Vernet. Vol. 12185. Proc. SPIE. 2022.
- [7] N. Schwartz et al. “Analysis and mitigation of pupil discontinuities on adaptive optics performance”. In: *Adaptive Optics Systems VI*. Ed. by L.M. Close, L. Schreiber, and D. Schmidt. Vol. 10703. Proc. SPIE. 2018.